Authors Version

EB-PVD alumina (Al_2O_3) as a top coat on 7YSZ TBCs against CMAS/VA infiltration: Deposition and reaction mechanisms.

R. Naraparaju, R. P. Pubbysetty, P. Mechnich and U. Schulz

Journal of the European Ceramic Society 38 (2018) 3333-3346

https://doi.org/10.1016/j.jeurceramsoc.2018.03.027

EB-PVD alumina (Al_2O_3) as a top coat on 7YSZ TBCs against CMAS/VA infiltration: Deposition and reaction mechanisms.

R. Naraparaju, R. P. Pubbysetty, P. Mechnich and U. Schulz

German Aerospace Centre (DLR), Institute of Materials Research, Cologne 51170, Germany

Abstract

Al_2O_3 was deposited as a top coat on a standard 7YSZ layer (or layers) by means of EB-PVD technique and the corresponding morphology of the Al_2O_3/7YSZ coatings was studied in detail. This multi-layer TBC system was tested against calcium-magnesium-aluminium-silicate (CMAS) recession by performing infiltration experiments for different time intervals from 5 min to 50 hours at 1250 ºC using two types of synthetic CMAS compositions and Eyjafjallajökull volcanic ash (VA) from Iceland. The results show that the studied EB-PVD Al_2O_3/7YSZ coatings react quickly with CMAS or VA melt and form crystalline spinel ($MgAl_{2-x}Fe_xO_4$) and anorthite ($CaAl_2Si_2O_4$) phases. The presence of Fe-oxide in the CMAS has been found to be key element in influencing the spinel formation which was proved to be more efficient against CMAS sealing in comparison to the Fe-free CMAS compositions. Even though a rapid crystallization was assured, shrinkage cracks in the EB-PVD alumina layer produced during the crystallization heat treatment have proven to be detrimental for the CMAS/VA infiltration resistance. To overcome these microstructural drawbacks, an additional alumina deposition method, namely reaction-bonded alumina oxide (RBAO), was applied on top of EB-PVD Al_2O_3. RBAO acts as a sacrificial layer forming stable reaction products inhibiting further infiltration.

1. Introduction

Modern gas turbines for energy and transportation particularly rely on high-temperature thermal barrier coatings (TBCs) for improved efficiency and power. Typically, TBCs are made up of ~7 wt. % Y_2O_3 stabilized ZrO_2 (7YSZ) ceramics [1-6]. A combination of porosity and very low thermal conductivity provides excellent high temperature insulation. TBCs are most commonly used as insulation material and to improve the durability of engine parts which also leads to an increase in the engine operating efficiency. The combustion temperatures of gas turbine engines are high enough to damage turbine blade alloy. Advanced cooling techniques utilize a combination of internal (forced convection, impingement cooling) and external (film cooling) systems, with the addition of TBCs, to increase efficiency and life time of different gas turbine engine parts. These TBCs are mainly deposited by electron beam physical vapor deposition (EB-PVD) or by air plasma spraying (APS) [7]. The EB-PVD top coats have inter-columnar porosity whereas the APS have porosity and cracks mainly running parallel to the interface. Apart from that, the siliceous minerals (CaO-MgO-Al_2O_3-SiO_2, commonly named CMAS), which are widely spread in the atmosphere and commonly identified in sand, runway debris, and volcanic ash, have a substantial effect on aircraft engines[8, 9] . The hot corrosion attack of these siliceous particles on TBCs eventually leads to premature failure. Since the infiltration of CMAS melts on standard 7YSZ TBCs brings detrimental effects on the lifetime of the coatings, many approaches for CMAS arrest have been proposed. Most of the CMAS mitigation strategies focus on the chemical reactions between the CMAS melt and the TBC to (i) stop the melt by crystallizing its main constituents (mostly silicates), and (ii) to block the melt by filling the pores and columnar gaps of the TBC with the new crystalized phases [10-16]. Alpha-alumina has been used as a CMAS resistant material on top of 7YSZ deposited by means of different deposition techniques[14, 17, 18]. In all cases, the alumina coating thickness achieved was not sufficient to guarantee a slow growing crystalline reaction layer which assures the protection against CMAS infiltration. There is no

available open literature on fabricating a columnar EB-PVD alumina top coat (with higher thickness) and infiltration tests on EB-PVD alumina coatings using CMAS/ VA. Thus, a better understanding of CMAS/VA with EB-PVD alumina interaction at high temperature can lead to significant benefits in the performance and lifetime extension for aero engines. The crystal structure and morphology of EB-PVD alumina columns entirely depend on process parameters, primarily substrate temperature, chamber pressure, and deposition rate. It is known from previous experiments and literature that during alumina evaporation an unstable melt pool and melt spitting is typically observed [19-23]. Therefore, fabricating crystalline EB-PVD alumina coatings is still challenging. The development of EB-PVD alumina layer as a CMAS resistant coating is discussed in this paper.

2. Experimental

Processing the EB-PVD alumina coatings

100-120 µm thick Al_2O_3 layers were deposited on the previously coated 150 µm thick 7YSZ TBCs via EB-PVD process (DLR coater ESPRI). To avoid damage of metallic substrates such as nickel based super alloys and bond coats during the high temperature infiltration tests for long duration, alumina substrates of 1 mm thickness were used as a base material to deposit Al_2O_3/7YSZ TBCs. A parameter study was conducted for EB-PVD alumina topcoat on 7YSZ and different runs were made and the resulting morphologies are explained in the section 3 as shown in Figure 1. The EB-PVD process was carried out by single source evaporation (using high purity Al_2O_3 ingots from Phoenix coating resources Inc., Florida, USA) under conventional rotating mode at different temperatures and pressures for the same rotation speed of 12 rpm and all the process parameters are given in Table 1.

Manufacturing of RBAO on top of EB-PVD alumina/7YSZ TBC

Reaction-bonded aluminum oxide (RBAO) topcoats were fabricated by a simple painting and firing process [24]. Spray-atomized Al powder (70 vol. %) and α-Al_2O_3 (30 vol. %) were used as starting materials for the RBAO processing. Five wt.-% of a soluble polymer (polyvinylpyrolidone) was added to the powder mixture. The powders were dispersed in isopropanol (30 wt. % solid content) and homogenized ultrasonically for 5 min. As coated EB-PVD alumina/7YSZ TBCs were cleaned ultrasonically in deionized water and dried carefully. The green coatings were deposited on the EB-PVD alumina topcoat TBCs by painting with a hairbrush (Figure. 2a). After drying, the coated samples were heat treated for 1 h at 1300°C with a heating rate of 10°C/min in isothermal furnace (Figure2b).

CMAS and Volcanic Ash Compositions

Two different CMAS compositions and one natural volcanic ash collected from Eyjafjallajökull volcano in Iceland were used for the infiltration studies (see Table 2). Both CMAS powders (CMAS 1 and UCSB CMAS) were artificially synthetized in the laboratory as used in previous studies [8, 25] .

Infiltration Experiments

Infiltration tests were carried out by depositing CMAS or VA on the top of Al_2O_3/7YSZ TBCs in the amount of 20 mg/cm^2. Infiltration tests were performed at 1250°C for short (5 min) and long durations (1 h and 10 h). Short term tests were performed in a cyclic furnace with an overall heating rate of 142 K/min, following isothermal exposure at 1250°C for 5 min and air quenching to room temperature. Long term CMAS/VA infiltration experiments were carried out isothermally in a Netzsch chamber furnace with a heating rate of 10 K/min.

Characterization

A Siemens D5000 diffractometer using Cu-Kα radiation with a secondary graphite monochromator was used for standard x-ray diffraction analysis (XRD). In-situ high-temperature XRD analyses were performed in a D8 Advance diffractometer with CuKα radiation and Lynxeye™ detector (Bruker AXS, Karlsruhe, Germany) using a Pt-strip-heated stage (HTK 16N, Anton-Paar, Graz, Austria). In-situ high temperature XRD was performed from 900°C to 1200°C in 50°C steps and 30 min holding times, respectively (Figure. 5). Microstructures of samples were analyzed by scanning electron microscopy (SEM) (DSM ultra 55, Carl Zeiss NTS, Wetzlar, Germany). Chemical microanalyses were carried out by energy-dispersive spectroscopy (EDS) (Inca, Oxford Instruments, Abingdon, UK).

3. Results

3.1. Fabrication of EB-PVD Al_2O_3 on top of 7YSZ TBCs

Figure.1 shows the SEM images of the manufactured alumina layers with respect to their coating parameters. It was known that in the typical coating temperature range for zirconia-based TBCs (900-1100°C) alumina undergoes phase transitions. As the melting point of alumina is considerably lower than that of zirconia, the substrate temperature during alumina evaporation was chosen to be approximately 890°C. Run 1 with sample temperature 890±5°C, a chamber pressure ($6*10^{-3}$ mbar) and with an ingot feed rate of 0.8 mm/min, shows that the morphology comprises irregular and asymmetrically distributed primary columns (see Figure. 1a). A high evaporation rate was observed with the beam energy of 65kW and as a result a highly porous coating was obtained with a deposition rate of 9 µm/min. These coatings were found to be very brittle with relatively low density which spalled instantaneously. As the desired alumina structure was not achieved in the Run 1, the coating was removed by grit blasting (corundum particles with 1.35 bar) and substrates were re-used in Run 2 and Run 3.

The evaporation rate was decreased by reducing the beam power to 44 kW keeping the same chamber pressure as in the case of Run 1. As a result, the sample temperature was reduced by 100°C in Run 2 and a deposition rate of 2.6 µm/min was achieved. These coatings show uniform growth of a columnar structure (Figure. 1b), but were brittle. Moreover, as shown in Figure 1(b), the transition at the 7YSZ/ alumina layer interface (note that the 7YSZ column tips were broken due to the grit blasting) was not smooth and the alumina column diameter continuously increases from root to top leading to a reduced number of columns. This has resulted in larger inter columnar gaps of around 4 µm which is shown as an inset in Figure 1(b). Run 3 was performed by maintaining the same sample temperature and beam energy but increasing the chamber pressure to $9*10^{-3}$ mbar and a deposition rate of 1.6 µm/min was achieved. The obtained coatings were of uniform thickness with the desired column density, as shown in Figure 1(c). Besides that the 7YSZ/alumina interface was found to be smooth and the alumina nucleation has almost followed the columnar microstructure of 7YSZ, although the nucleation of alumina took place on the grit blasted surface which is shown in high magnification in Figure 1(e). The column width has been reduced in comparison to the Run 2 and the shape of the columns remained uniform throughout the coating thickness which has resulted in reduced inter-columnar gaps.

Run 4 was performed on as coated EB-PVD 7YSZ samples at slightly increased sample temperature (around 30°C) and same chamber pressure as in Run 3, but the deposition time was increased to 45 minutes to get a thick coating. The deposition rate achieved in this run was found to be 2.4 µm/min. The main difference between the Run 3 and 4 was the 7YSZ surface condition, the former being grit blasted and the latter as coated. The coatings show regular growth of columns with less inter-columnar

gaps. A uniform thickness with suitable visible density of the coating was achieved. In addition the 7YSZ/ alumina interface was found to be smooth with a perfect transition as shown in Figure 1 (f). Coatings with 110 µm thick alumina top layers achieved in Run 4 were used for all the further infiltration tests. No spitting and evaporation problems were detected during the coating process. Excellent adhesion of alumina on 7YSZ except in Run 1 was observed as expected from the well-known good compatibility and adhesion between alumina TGO and 7YSZ or alumina substrates and 7YSZ.

3.2. EB-PVD alumina characterization and phase transition

As coated EB-PVD alumina coatings were amorphous in nature with a little contribution from cubic gamma phase. It is known from the literature that the phase transition from amorphous to crystalline α-alumina occurs in the temperature range of 900°C to 1200°C [20, 26, 27]. In situ high temperature XRD analysis was performed on the alumina layers and the corresponding phase changes are shown in Figure 3. Changes in α-alumina peak intensities were very low in the temperature range between 900-1050°C and high intensity sharp peaks were only observed at 1100°C for 30 min. No meta-stable phases were found in the XRD patterns. Thus, this temperature was taken for further heat treatment of as-coated samples to obtain thermodynamically stable α-alumina topcoats. During the pre-heat treatment heavy sintering of the alumina coating was observed. SEM surface and cross-sectional micrographs in Figure 4 show the drastic change in microstructure before and after heat treatment. As-coated samples at room temperature have a fully dense coating with very thin inter-columnar gaps (see Figure. 4(a) & (b)). After the heat treatment, as shown in Figure 4 (c) shrinkage cracks have appeared. In the cross-sectional analysis these cracks are clearly visible in Figure 4(d). In addition, a slight change in the intra columnar microstructure was also observed after the crystallization treatment as shown in Figure 4(b) and (d). Alumina columns were found to be more porous after pre-heating than after as coated which is assumed to be due to the crystallization of amorphous alumina. The columns were also found to be shrinked after the heat treatment. The interface adhesion was found to be unaffected by the heat treatment as can be seen in Figure 4(b) and (d). No cracks or delamination were observed at the interface and the adhesion between 7YSZ layer and alumina was found to be un-effected by the sintering process.

3.3. CMAS/VA Infiltration Tests

Phase formation of α-Al_2O_3 and CMAS/VA powder mixtures

Al_2O_3 is expected to react firmly with all the CMAS/VA variants and to form new crystalline phases. Alumina powder was mechanically removed from the coatings and used for phase identification. In order to identify all potential reaction products, powder mixtures consisting of 60 wt. % of CMAS/VA and 40 wt. % of alumina were prepared (uniformly mixed in a mortar) and isothermally heat treated at 1250°C for 10 h, respectively. Figure. 5 shows the XRD pattern of the alumina/CMAS/VA powder mixture. Two main common crystal phases are identified as anorthite ($CaAl_2Si_2O_8$) (An) and (Mg, Al, Fe)-spinel $Mg(Al_{2-x}Fe_x)O_4$ (Sp). These phases i.e., anorthite (An) and spinel (Sp) exhibit CMAS sealing property for alumina coatings. Anorthite (An) exhibits the highest peak intensity for UCSB CMAS, followed by CMAS 1 and Iceland ash. The second common phase, identified as spinel (Sp), exists in CMAS 1 and Iceland ash. In UCSB CMAS/alumina mixture, an additional phase is identified as melilite (Me, ($Ca_2(Mg_{0.25}Al_{0.75})(Si_{1.25}Al_{0.75}O_7)$) which might be left over CMAS glass. In the case of Iceland ash, pseudobrookite (Ps, (Fe_2TiO_5)) containing Fe and Ti was identified.

Short Term Infiltration

In order to identify the CMAS/VA initial crystallization products short term infiltration tests for 5 min were conducted on the EB-PVD alumina coatings at 1250°C. Figure. 6 shows the overall SEM cross-sectional view and the Ca element mapping for all the CMAS/VA infiltrated samples. In all the cases especially in larger cracks, CMAS/VA has reached the 7YSZ interface but no reaction with 7YSZ was observed. It is clear that these larger gaps offer no resistance to the infiltration but the time was too short for the yttria dissolution in the melt. Figure. 7(a) shows the high magnification image of the reaction zone between CMAS 1 and alumina. Based on compositions measured by EDS and the XRD powder mixture results "most likely" formed crystal phases have been identified. The reaction layer which partially seals the inter-columnar gaps was identified as spinel (Sp). Another CMAS crystalizing product on top of spinel was identified as anorthite (An). The light gray contrasted product at the top of the image and at the center of the columnar gaps represents the residual CMAS glass (g). The total reaction layer thickness was around 2 µm. Table 3 provides a summary of all the elemental composition and the corresponding phases.

Figure. 7(b) corresponds to the initial crystallization of UCSB CMAS and the Al_2O_3 layer. The flat crystalline layer growing on the top of alumina is identified as anorthite (An). The further crystalline product on top of anorthite is identified as melilite (Me). The total reaction layer thickness was found to be 2 µm and similar to that of CMAS 1. The chemical composition of the products labelled in the image is shown in Table 4 along their phase identification (comparing EDS and XRD results). Figure. 7(c) shows the reaction zone of Iceland VA/alumina interface. The initial reaction product is spinel which was also observed in CMAS 1. There exists anorthite layer between the spinel and the top glass layer. The spherical grains in the glass are identified as pseudobrookite (Ps) containing iron and titanium. The EDS spot analysis reveals the higher content of iron in pseudobrookite as shown in Table 5. The reaction layer thickness was found to be 2-3 µm. In all the three studied CMAS/VA cases, a reaction layer of 2-3 µm thickness has formed after 5min at 1250°C. However, in all cases CMAS/VA has infiltrated through the wider inter-columnar gaps.

Long Term Infiltration

The long term isothermal infiltration tests were performed to study the coating infiltration resistance and reaction layer growth over increased periods of time (1 and 10 hours). The total reaction layer thickness is measured from the starting point of spinel occurrence to the end of unreacted alumina top coat.

Figure. 8 shows the elemental mapping of the reaction layer formed at the CMAS 1/Al_2O_3 interface depicting the reaction layer growth from 1 h to 10 h. It is immediately apparent from the elemental mapping that the (Mg, Al, Fe) -spinel layer (Sp) grows with respect to time and is the only reaction layer that develops at the interface. Another crystalline layer consisting of anorthite (An) was formed on top of the spinel layer**.** The chemical composition of the products after 10 h is shown in Table 3. From the elemental mapping it can be clearly seen that the CMAS has completely infiltrated EB-PVD alumina through the wider cracks and has reacted with the 7YSZ columnar tips at the interface. However, the infiltration could not proceed through the circumference of the alumina columns (i.e. horizontally) as the formed spinel layer has assured the sealing of the CMAS. Red lines in the micrographs separate the reaction layer from the unreacted alumina at the CMAS 1/alumina interphase. The reaction products spinel (Sp) and anorthite (An) are clearly visible. The thickness of the reaction layer has increased from 5 µm to 12 µm after 1 and 10 h heating, respectively, while the reaction products did not exhibit a large difference in their chemical composition after 10 h except the iron and alumina content in the spinel. Furthermore, reaction layers do not show significant morphological changes over time. CMAS 1 has completely infiltrated through the underlying 7YSZ layer.

Figure. 9 shows the reaction layer growth on top of the UCSB CMAS/alumina interface after 1 h. and 10 h. of isothermal heating at 1250°C. From the elemental mapping, it is observed that the infiltration effect is larger compared to CMAS 1 where not only wide cracks were infiltrated but also infiltration was strong along the circumference of the columns (i.e. in the horizontal direction). The CMAS has also infiltrated completely through the 7YSZ columns. Anorthite was formed next to the alumina layer, melilite has formed on top of anorthite and the residual CMAS glass stayed on top of the melilite. Table 4 provides a summary of all the elemental composition and the corresponding phases after 10 h. The influence of those wider gaps on the infiltration behaviour of CMAS or VA is discussed below. No spinel formation at the interface was observed (Absence of Fe, Mg enrichment at the interface).The formed reaction products have undergone a minor change in their chemical composition with respect to time and a significant growth of the reaction layer with an increase in the thickness from 5 µm to 8 µm after 1 h and 10 h was observed. Figure. 10 shows the infiltration scenario with the respective elemental mapping after 1 h and 10 h of the VA at 1250°C. A uniform (Mg,Al,Fe)-spinel layer was formed on top of the alumina coating followed by a thin anorthite layer. The VA ash has completely infiltrated the EB-PVD alumina via cracks and underlying 7YSZ layer through the inter-columnar gaps. However, the severity of its attack was less compared to the UCSB CMAS. An increase of the reaction layer thickness from 3 µm to 7 µm was observed after 1 h and 10 h, respectively. Large iron and titanium rich pseudobrookite crystals (Ps) were observed on the top of spinel layer. Pseudobrookite crystals significantly grow over time and the corresponding chemical compositional change of Fe and Ti is presented in Table 5. The residual CMAS glass remains present on top of all the layers in both the short and long term isothermal tests. Reaction layer growth of alumina with all the CMAS/VA with respect to time is drawn in Figure 11.

3.4. CMAS Infiltration Tests on RBAO Alumina/7YSZ

In the previous sections it was noticed that the EB-PVD alumina exhibits a high reactivity with CMAS/VA and rapidly forms CMAS arresting products. However, sinter cracks that had been developed during the pre-heat treatment have allowed the CMAS/VA to locally fully infiltrate. To overcome the microstructural shrinkage effects, a further alumina layer was applied by means of the RBAO method. Alpha-Al_2O_3 was created during the application process itself because of the heat treatment at 1300°C. Figure. 12 shows the 20-25 µm thick RBAO layer on top of EB-PVD alumina. The microstructure with no macroscopic crack formation or RBAO coating - alumina topcoat de-bonding was obtained during the process. For a preliminary assessment, CMAS 1 has been tested on RBAO/EB-PVD-alumina/7YSZ for 10 h, 20 h, and 50 h at 1250°C. The corresponding EDS mappings of calcium are shown in Figure. 13. No infiltration within the EB-PVD columnar gaps was found even after 50 h of testing and the top RBAO has sealed the coating against CMAS 1. The main crystalline phase which blocks the CMAS infiltration is the dense (Mg, Al, Fe)-spinel layer (Sp) formed on top of EB-PVD alumina after 50h is shown in Figure 14. The other phase was found to be anorthite (An) as observed in all the other cases in this study. As time progresses, a growth of the reaction layer was observed and the total RBAO layer with initial thickness of 20-25 µm was eventually consumed during the reaction process. Since the final reaction layer thickness was found to be 36 µm after 10 h, 39 µm for 20 h, and 44 µm after 50 h of isothermal heating, the reaction layer originating from EB-PVD alumina was growing by about 12-20 µm in the time span of 10 and 50 h, but it was still protective.

4. Discussion

Alumina has been widely recognized as a sacrificial top-coating for YSZ TBC due to its ability to shift the CMAS composition in order to promote crystallization and blocking further CMAS melt infiltration[14, 17, 18]. However, the deposition of Al_2O_3 via EB-PVD technique has been an issue of

concern. The morphology of an EB-PVD columnar microstructure strongly depends on the process parameters [6, 23, 28-30] such as source material, deposition rate, pressure, part rotation speed, temperature and so on. Moreover, the coating morphology is a function of the melting point of the coating material and the temperature of the substrate material being coated. In Run 1, although the used substrate temperature and beam powers were in the range of typical yttria-zirconia system, a higher evaporation rate was observed which has resulted in a porous brittle coating. From the literature it is known that in the case of 7YSZ, a higher temperature leads to a higher density of the coating and the higher pressure causes lower density [31, 32]. Such kind of data was not available for the alumina deposition and to reduce the alumina evaporation rate and to achieve a more suitable coating quality, the beam power was reduced to 44 kW and the substrate temperature to 790°C in Run 2. A dense coating was achieved but the rough 7YSZ surface (grit blasted) has played a major role in the nucleation of the alumina layer and the shape of the alumina columns. It is well known that the surface finish of the substrate plays a significant role in defining the microstructure of EB-PVD columns. On a polished bond coat surface the columnar growth of 7YSZ was found to be uniform and dense whereas grit blasted surfaces had resulted in porous and non-uniform coatings[32]. In another study it was shown that a grit blasted EB-PVD 7YSZ surface has experienced a slight disruption of the columnar growth upon re-deposition whereas a polished surface has a fine grained zone with subsequent coarsening of the columns [33]. In contrary, the initial nucleation of alumina was found to be not following the underlying 7YSZ columns in Run 2. It is expected that by increasing the chamber pressure the density of the coating should decrease at the lower substrate temperatures which might result in different columnar microstructure. Run 3 was performed with a slightly high chamber pressure and consequently a variation in the alumina columnar microstructure was observed. Thin and uniform columns with almost smooth transition from the 7YSZ layer were obtained (Figure. 1f). The drop in the deposition rate (from 2.6 to 1.6 µm/min), however, contradicts the general tendency where higher deposition rate is obtained with higher pressure (in case of EB-PVD 7YSZ) as discussed in the literature [31, 33]. This heterogeneity effect can be attributed to the entirely different evaporation behavior of alumina and the role of 7YSZ surface roughness. A slight increase in the substrate temperature facilitated the higher deposition rate in Run 4 where the ability for diffusion of condensed particles got increased. Even though 30°C rise might be considered as very small, having the 100°C operational window for alumina deposition this rise could influence the deposition rate considerably. In addition, run 4 was much longer than all other runs and the final columnar microstructure needs some time to get established. Consequently, coating density may vary along the thickness, and variations in alumina thickness may than translate into density variations and hence into a different deposition rate. The as coated EB-PVD 7YSZ surface with its pyramidal shaped column tips has not shown a big influence on the final microstructure of EB-PVD alumina columns. The transition at the interface was slightly better than that of a grit blasted interface. In run 3, i.e. the surface roughness plays an important role on the nucleation of the columns but at the same time temperature and pressure can compensate that effect with advancing coating thickness. Having known that in the used temperature ranges alumina could only be coated as an amorphous layer, a higher deposition temperature could not be applied due to the so far explained reasons. As a consequence an additional crystallization treatment was inevitable and a pre-heat treatment was conducted at 1100°C. The annealing resulted in the desired alpha alumina phase but produced at the same time unfavourable shrinkage cracks in a mud-type crack arrangement, similarly to previous observations [21]. It is well known that the alumina undergoes phase transitions from highly disordered cubic close packed transition gamma alumina lattice to more ordered cubic close packed theta alumina to the final hexagonal close packed alpha alumina lattice at high temperatures. This alpha alumina phase transitions occurs by nucleation and growth which results in large spacing between nucleation events and formation of micrometer scale pore channels [34]. Comparatively higher porosity in the alumina

columns after the heat treatment might be occurring due to the phase transition of alumina. In the current high temperature in-situ XRD experiments presence of such transition alumina was not found, most likely because of the faster heating rate and shorter holding time at each temperature. Alpha alumina was observed at temperatures equal or above 1050°C. If the substrate would be a superalloy instead of the alumina substrates used here for experimental reasons, and alumina is coated as a topcoat, the coefficient of thermal expansion (CTE) mismatch would be substantial and it can lead to spallation of the top coat. Having these shrinkage cracks in the alumina top layer could compensate the thermal mismatch stresses which induce the delamination. The influence of those wider gaps on the infiltration behaviour of CMAS or VA is discussed below. If the alumina is stiffened by the CMAS infiltration, the CTE mismatch would play a major role on the durability of the layer.

From the existing knowledge it is well known that chemical composition of CMAS varies significantly from a geographical region to the other [9]. CMAS chemical composition plays an important role in defining the reaction products with TBCs at high temperatures [35]. Especially the reported CMAS arresting phases such as apatite, garnets and spinels depend on the FeO, SiO_2 and CaO content in the CMAS and the presence of FeO/Fe_2O_3 in the CMAS promotes the crystallization of the glass and forms different reaction products [16]. Hence two synthetic CMAS compositions having similar CaO and SiO_2 content but one with FeO were used in this study. With respect to CMAS, volcanic ashes (VA) generally contain relatively high amount of SiO_2 and are mostly amorphous and the amount of SiO_2 influences heavily the viscosity of the melt. The reactivity of alumina with a silica-rich deposit (VA) is tested in this study. VA also consist larger amounts of FeO and TiO_2 compared to CMAS 1 which might play different role in defining the reaction behavior with alumina. In all the conducted infiltration tests it was found out that the dissolution of Al into the CMAS/VA-melt quickly generates a stable phase that seals the columnar gaps preventing further infiltration as seen in the literature [14, 17, 18]. This reaction layer grows with respect to time by consuming CMAS/VA and alumina from the coating and ultimately the growth kinetics is one of the defining factors for the protective nature of the TBC material. The reaction layer growth on alumina coating for all the used CMAS/VA compositions over time is shown in Figure. 11. There is a rapid reaction layer growth in between 0-5 min (2-3 µm) which is stabilizing after 1 h (4-5 µm) in all the cases. The reaction layer growth is governed by several factors such as coating porosity, CMAS/VA melt viscosity, temperature, and time. Once a dense reaction layer is formed, growth is sustained by the availability of the melt and infiltration through the reaction layer. Infiltration through the layer is influenced by the presence of cracks, pores formed during the reaction, diffusivity of the species, and the melt viscosity [8, 36]. Combining all these effects, the largest reaction layer growth after 10 h is observed for CMAS 1 (12 µm) followed by UCSB CMAS (8 µm) and VA (7 µm). The reaction scenario for Alumina layers with all CMAS/VA compositions is schematically presented in Figure 15.

In case of CMAS 1, the first and fastest reaction product which grows at the interphase is a (Fe, Mg, Al) spinel (Sp) which crystallizes the glass in areas such as the alumina topcoat surface, column arms and minor cracks/gaps. This was observed even after 5 min test as shown in Figure 7 & 15(upper part). This layer grows by consuming significant amounts of Fe and Mg from the CMAS 1 melt. For CMAS 1 the spinel is the most stable phase present in the reaction layer, which grows with respect to time by consuming Al from the coating assuring the sealing property as shown in Figure 15 (lower part). The constant growth of the spinel phase is believed to be due to the presence of high amounts of Mg and Fe in CMAS 1. The rise in the alumina content in the spinel after 10 h confirms the continuous intake of alumina in the spinel as shown in Table 3. After the spinel formation, the remaining Ca and Si within CMAS react with alumina to form anorthite (An) on top of the spinel and the chemical composition of the anorthite remained constant during the time. CMAS was found to crystallize into anorthite and spinel by chemically interacting with α-alumina has been reported in literature[18] and

was found in the present powder mixture annealing experiments as well. The anorthite phase is known for its stability which was reported to provide sealing properties[17]. However, in the present case the anorthite phase was only found on top of the reaction layer as a secondary reaction product without sealing capability since a large reservoir of melt is still available. EB-PVD Al_2O_3 coatings exhibited cracks and gaps after the crystallization heat treatment. The wide gaps could be easily penetrated by all deposits, act as a reduced barrier for the penetration of the CMAS melt and this behavior was observed immediately after 5 mins. However, due to the very short time the reaction products did not evolve uniformly within the cracks. After few hours of infiltration time, the CMAS 1 has penetrated the whole alumina layer and the 7YSZ layer. A clear distinction between the reaction products within the cracks could be observed. A spinel layer has formed at the boundaries of the cracks and an anorthite layer next to it followed by the rest glass similar to the surface reaction. The infiltrated CMAS 1 has reacted with the 7YSZ columnar tips and the feather arms, while dissolution of yttria causes destabilization of tetragonal zirconia which is illustrated in Figure 15 as discussed in the literature [8, 15]. Wherever these cracks were not present the formed spinel layer has sealed the CMAS infiltration and that clearly shows the protective nature of spinel layer.

UCSB CMAS forms anorthite (An) as a reaction product directly on top of alumina as well as in the cracks even after 5 mins. As seen in the Figure 6 and 15, the cracks were used as free paths by the CMAS and as the infiltration time has progressed the reaction scenario became clear and an increase in the anorthite layer thickness was observed. Infiltration has progressed through the cracks up to the 7YSZ interface and also through the whole 7YSZ layer. However, the anorthite layer which was formed on the alumina surface was not as protective as the spinel layer as in the case of CMAS 1. The excess infiltration in addition to the cracks in the alumina layer as observed in Figure 9, supports the idea that anorthite could not form uniformly at the CMAS/alumina interface and the molten glass was using these gaps to infiltrate. The other crystalline product melilite (Me) which was formed discretely as a byproduct on top of anorthite consists all the elements that CMAS glass has and probably cannot provide protective sealing effect. The magnesia content in the melilite phase has increased substantially after 10 h as shown in Table 4 and the anorthite phase has been stabilized. The absence of Fe in UCSB CMAS does not provide enhanced spinel formation and the magnesia has been segregated in to melilite with the remaining glass; as a result alumina could not be sealed by a protective spinel layer restricting the infiltration. Another interesting observation was the growth of anorthite crystals within the cracks. These crystals were almost sealing the cracks with smaller glass pockets inside as shown in Figure 9 and 15 (lower part). The reason for this behavior could be due to a slow reaction rate and anorthite phase needs longer annealing times. i.e. once the whole alumina and 7YSZ layers were infiltrated the glass accumulated within the cracks has accommodated the continuous alumina supply from the coating and crystalized into a thick anorthite. From the results it can be concluded that Fe is a key element enhancing crystallization of the spinel phase. As a consequence UCSB CMAS has infiltrated through the circumference of the columns (i.e., thicker deposits of Ca, Si compared to the CMAS1/VA) along with the infiltration within the inter-columnar gaps up to the underneath 7YSZ layer. Presence of globular particles at the 7YSZ interface proves that the 7YSZ layer has undergone reaction with the UCSB CMAS similar to the CMAS 1 case.

In the case of VA, the reaction has proceeded with a quick formation of spinel generating an initial sealing against the melt after 5 mins as shown in Figure 7 and 15 (upper part). A thin anorthite layer was formed on top of the spinel layer similar to that of CMAS 1. In contrast to the CMAS 1, VA has formed an additional phase pseudobrookite within the cracks as well as in the left over glass on top. The growth rate of the spinel layer is relatively slow, when compared to CMAS 1. Two reasons may explain this observation: First, the viscosity of VA is higher in comparison with CMAS 1 [16]. Second, Fe and Ti which were present in higher amounts (around 2 times) in VA were partially

consumed by the other crystalline phase pseudobrookite (Ps). This effect can be witnessed by the increase in the pseudobrookite crystal size after 10 h (Figure 10 and 15). A noticeable change in chemical composition of pseudobrookite with respect to time has been observed. An increase in Ti and a decrease in Fe content was seen (see Table 5), where the Fe content from glass acts as a sink for stabilizing spinel layer on top from 1h to 10 h. It is clear that the pseudobrookite phase did not involve alumina and therefore its crystallization was a product of the changes in chemistry as the reaction with alumina proceeds. This may not play a major role in the melt arrest mechanism. The noticeable difference in the spinel composition of the VA case (higher iron oxide to alumina ratio compared to CMAS 1) confirms that FeO has a preference to stabilize the spinel layer and promotes its formation. Infiltration has proceeded to the 7YSZ layer with respect to the time and the reaction was similar to the other cases.

The pure chemical criterion for the selection of TBCs that are resistant to CMAS/VA attack having a quick reaction followed by the crystallization of the melt is not sufficient when it comes to a real coating. The coating microstructure plays an equal and important role and this fact is proven in this study as the EB-PVD alumina offers little resistance to the infiltration due to its microstructural effects. As an alternative, new approach a RBAO top-coat was applied on EB-PVD alumina to diminish detrimental effects of the shrinkage cracks. An important benefit of the RBAO manufacturing process is the oxidation-induced volume expansion of Al, which reduces or even fully compensates sintering related shrinkage of the underlying EB-PVD alumina and finally prevents coating crack formation [24]. RBAO has formed same CMAS arresting products with the CMAS 1 as in case of EB-PVD alumina layer as expected. The main difference between EB-PVD and RBAO alumina coatings is its microstructure where RBAO offers high surface area of pores which are distributed uniformly over the surface compared to the inter columnar gaps (and shrinkage cracks) in case of EB-PVD. This allows the CMAS 1 to readily infiltrate more rapidly and react uniformly and form a quick sealing spinel layer. The RBAO top-coat was being uniformly infiltrated (see Figure 13) initially but by that time it has also rapidly reacted with CMAS melt and induced spinel crystallization. From the literature it is known that the most efficient TBC coating in arresting CMAS was Gadolinium zirconate and it has formed a reaction layer of 30 µm when it is subjected to a heat treatment for 4 h at 1300°C [12, 37]. In comparison, a maximum infiltration depth of 41 µm was observed after 50 h at 1250°C in RBAO/EB-PVD alumina against CMAS in this study. No CMAS further infiltration into the underlying 7YSZ layer was observed. This clearly states that the RBAO is probably another reliable processing method/material for CMAS mitigation. Currently ongoing research concentrates on (i) reducing the manufacturing temperature of the RBAO in order to avoid the expected damage to the underlying metal when using the currently applied 1300°C, (ii) increasing the RBAO thickness, and (iii) applying it directly on the 7YSZ TBC. In the future an assessment of performance and the spallation behavior of such sacrificial RBAO top-coats have to be made by performing furnace cycle and thermal cycling tests.

5. Conclusions

Al_2O_3 has been successfully deposited on top of 7YSZ using EB-PVD with a favourable columnar morphology. As the as-coated alumina is amorphous an additional heat treatment was needed to establish the stable alpha alumina phase. The following conclusions can be made based on this study.

1. Substrate temperature and the chamber pressure have a great influence on the EB-PVD alumina columnar microstructure, especially on the inter-columnar porosity and the column thickness. A rough 7YSZ surface influences the nucleation of alumina layer at the interface and the growth of columns. Selection of right temperature and the pressure can counterpart the rough surface and control the alumina nucleation to have a smoother interface.

2. Alumina coatings exhibited good CMAS/VA resistance by forming melt arresting products (i.e., spinel ($MgAl_{2-x}Fe_xO_4$ and anorthite ($CaAl_2Si_2O_8$)). The reaction products seal smaller gaps against infiltration and generate a uniform reaction layer at the TBC/melt interface which exhibited a minimal growth with time. However, the melt infiltration could not be mitigated in larger cracks that are formed due to the crystallization of the amorphous alumina coatings.

3. The Fe content in CMAS/VA plays a significant role in forming a (Mg, Al, Fe)-spinel acting as major sealing phase. In the case of CMAS 1 and Iceland VA which contain high amounts of Fe, the diffusion of Al into the Fe rich glass exhibits a higher activity in generating spinel whereas the absence of Fe in UCSB CMAS prevented the formation of spinel.

4. Additional reaction-bonded alumina (RBAO) top-coats provide a favourable porosity network and rapidly react with CMAS, finally completely preventing melt infiltration into the TBC. Therefore, RBAO is considered a potential sacrificial top coat for mitigating TBC damage by deposits.

Acknowledgments:

The authors express their gratitude to D. Peters and J. Brien for manufacture of TBCs, as well as A. Handwerk for providing technical support for thermal test implementation. Additionally, the authors thank J Gomez Chavez for his assistance in critical input and discussions related to the project. The authors thank the German Science Foundation (DFG) for funding this project (Nr: SCHU 1372/5-1).

References:

1. D. R. Clarke, M. Oechsner, and N. P. Padture, 'Thermal-barrier coatings for more efficient gas-turbine engines', MRS bulletin **37** (10) (2012) 891-898.

2. X. Q. Cao, R. Vassen, and D. Stoever, 'Ceramic materials for thermal barrier coatings', Journal of the European Ceramic Society **24** (2004) 1-10.

3. R. Darolia, 'Thermal barrier coatings technology: critical review, progress update, remaining challenges and prospects', International Materials Reviews **58** (2013) 315-348.

4. C. G. Levi, 'Emerging materials and processes for thermal barrier systems', Current Opinion in Solid State and Materials Science **8** (1) (2004) 77-91.

5. R. A. Miller, 'Thermal barrier coatings for aircraft engines: history and directions', Journal of Thermal Spray Technology **6** (1) (1997) 35-42.

6. A. F. Renteria, B. Saruhan, U. Schulz, H. J. Raetzer-Scheibe, J. Haug, and A. Wiedenmann, 'Effect of morphology on thermal conductivity of EB-PVD PYSZ TBCs', Surface and Coatings Technology **201** (2006) 2611-2620.

7. S. Sampath, U. Schulz, M. O. Jarligo, and S. Kuroda, 'Processing science of advanced thermal-barrier systems', MRS Bulletin **37** (2012) 903-910.

8. R. Naraparaju, U. Schulz, P. Mechnich, P. Döbber, and F. Seidel, 'Degradation study of 7wt.% yttria stabilised zirconia (7YSZ) thermal barrier coatings on aero-engine combustion chamber parts due to infiltration by different CaO-MgO-Al_2O_3-SiO_2 variants', Surface and Coatings Technology **260** (2014) 73-81.

9. C. G. Levi, J. W. Hutchinson, M.-H. Vidal-Sétif, and C. A. Johnson, 'Environmental degradation of thermal-barrier coatings by molten deposits', MRS Bulletin **37** (2012) 932-941.

10. A. Aygun, Novel thermal barrier coatings (TBC) that are resistant to high temperature attack by CaO-MgO-Al_2O_3-SiO_2 (CMAS) glassy deposits, Acta Materialia, 55 (20) (2008) 6734-7745.

11. J. M. Drexler, A. D. Gledhill, K. Shinoda, A. L. Vasiliev, K. M. Reddy, S. Sampath, and N. P. Padture, 'Jet engine coatings for resisting volcanic ash damage', Advanced Materials **23** (2011) 2419-2424.

12. S. Krämer, J. Yang, and C. G. Levi, 'Infiltration-inhibiting reaction of gadolinium zirconate thermal barrier coatings with CMAS melts', Journal of the American Ceramic Society **91** (2008) 576-583.

13. A. R. Krause, H. F. Garces, B. S. Senturk, and N. P. Padture, '$2ZrO_2 \cdot Y_2O_3$ thermal barrier coatings resistant to degradation by molten CMAS: Part II, Interactions with sand and fly ash', Journal of the American Ceramic Society **97** (2014) 3950-3957.

14. A. K. Rai, R. S. Bhattacharya, D. E. Wolfe, and T. J. Eden, 'CMAS Resistant Thermal Barrier Coatings (TBC)', International Journal of Applied Ceramic Technology **7** (2010) 662-674.

15. U. Schulz and W. Braue, 'Degradation of $La_2Zr_2O_7$ and other novel EB-PVD thermal barrier coatings by CMAS (CaO-MgO-Al_2O_3-SiO_2) and volcanic ash deposits', Surface and Coatings Technology **235** (2013) 165-173.

16. R. Naraparaju, J. J. Gomez Chavez, U. Schulz, and C. V. Ramana, 'Interaction and infiltration behavior of Eyjafjallajökull, Sakurajima volcanic ashes and a synthetic CMAS containing FeO with/in EB-PVD ZrO_2-65 wt%Y_2O_3 coating at high temperature', Acta Materialia **136** (2017) 164-180.

17. X.-f. Zhang, K.-s. Zhou, W. Xu, B.-Y Chen, J.-b. Song, and M. Liu, 'In situ synthesis of α-alumina layer on thermal barrier coating for protection against CMAS ($CaO–MgO–Al_2O_3–SiO_2$) corrosion', Surface and Coatings Technology **261** (2015) 54-59.

18. P. Mohan, B. Yao, T. Patterson, and Y. H. Sohn, 'Electrophoretically deposited alumina as protective overlay for thermal barrier coatings against CMAS degradation', Surface and Coatings Technology **204** (2009) 797-801.

19. U. Leushake, 'Design, Herstellung und Lebensdauer gradierter elektronenstrahlgedampfter Wärmedämmschichten im System Aluminiumoxid, Zirkonoxid. Aachen, RWTH, 2001.[PhD thesis]

20. U. Leushake, T. Krell, U. Schulz, M. Peters, W. Kaysser, and B. Rabin, 'Microstructure and phase stability of EB-PVD alumina and alumina/zirconia for thermal barrier coating applications', Surface and Coatings Technology **94** (1997) 131-136.

21. T. Krell, Thermische und thermophysikalische Eigenschaften von elektronenstrahlgedampften chemisch gradierten Al_2O_3/PYSZ-Wärmedämmschichten. Fortschritt-Berichte VDI, Aachen, RWTH, 2001.[PhD thesis]

22. T. Krell, U. Schulz, M. Peters, and W. Kaysser, EB-PVD Zirconia Thermal Barrier Coatings with graded Al_2O_3-PYSZ Interlayers In: Functionally Graded Materials 2000 Ceramic Transactions,114, The American Ceramic Society, Westerville OH, USA, 2001.

23. T. Krell, U. Schulz, M. Peters, and W. Kaysser, Influence of Various Process Parameters on Morphology and Phase Content of EB-PVD Thermal Barrier Coatings, 5th European Conference on Advanced Materials and Processes and Applications "Materials, Functionality & Design", Maastricht, NL 21.04. - 23.04.1997.

24. P. Mechnich, W. Braue, and H. Schneider, 'Multifunctional Reaction Bonded Alumina Coatings for Porous Continuous Fiber Reinforced Oxide Composites', International Journal of Applied Ceramic Technology **1** (4) (2004) 343-350.

25. S. Krämer, J. Yang, C. G. Levi, and C. A. Johnson, 'Thermochemical interaction of thermal barrier coatings with molten CaO–MgO–Al_2O_3–SiO_2(CMAS) deposits', Journal of the American Ceramic Society **89** (10) (2006) 3167-3175.

26. M. I. F. Macêdo, C. A. Bertran, and C. C. Osawa, 'Kinetics of the γ→ α-alumina phase transformation by quantitative X-ray diffraction', Journal of materials science **42** (8) (2007) 2830-2836.

27. T. Shirai, H. Watanabe, M. Fuji, and M. Takahashi, 'Structural properties and surface characteristics on aluminum oxide powders', Annual report of the Ceramics Research Laboratory, Nagoya Institute of Technology 9 (2009) 23-31.

28. R. Naraparaju, M. Huttermann, U. Schulz, and P. Mechnich, 'Tailoring the EB-PVD columnar microstructure to mitigate the infiltration of CMAS in 7YSZ thermal barrier coatings', Journal of the European Ceramic Society **37** (1) (2017) 261-270.

29. U. Schulz, T. Krell, U. Leushake, and M. Peters. Graded design of EB-PVD thermal barrier coatings system. Proceedings of AGARD Workshop on Thermal Barrier Coatings (Aalborg, DK, 1997.

30. A. F. Renteria, A small-angle scattering analysis of the influence of manufacture and thermal induced morphological changes on the thermal conductivity of EB-PVD PYSZ Thermal barrier coatings. Aachen, RWTH, 2003.[PhD thesis]

31. U. Schulz, J. Münzer, and U. Kaden. Influence of deposition conditions on density and microstructure of EB-PBD TBCs. 26th Annual Int. Conf. on Advanced Ceramics & Composites, Cocoa Beach, 13-18 January (2002).

32. D. V. Rigney, R. Viguie, D. J. Wortman, and D. W. Skelly, 'PVD thermal barrier coating applications and process development for aircraft engines', Journal of Thermal Spray Technology **6** (2) (1997) 167-175.

33. U. Schulz, H. J. Raitzer-Scheibe, B. Saruhan, and A. F. Renteria, 'Thermal conductivity issues of EB-PVD thermal barrier coatings', Materialwissenschaft Und Werkstofftechnik, **38** (9) (2007) 659-666.

34. E. Yalamaç, A. Trapani, and S. Akkurt, 'Sintering and microstructural investigation of gamma–alpha alumina powders', Engineering Science and Technology, an International Journal, **17** (1) (2014) 2-7.

35. D. L. Poerschke, T. L. Barth, and C. G. Levi, 'Equilibrium relationships between thermal barrier oxides and silicate melts', Acta Materialia, **120** (2016) 302-314.

36. R. Naraparaju, P. Mechnich, U. Schulz, and G. C. Mondragon Rodriguez, 'The Accelerating Effect of $CaSO_4$ Within CMAS ($CaO-MgO-Al_2O_3-SiO_2$) and Its Effect on the Infiltration Behavior in EB-PVD 7YSZ', Journal of the American Ceramic Society Ceramic Society, **99** (2016) 1398-1403.

37. P. Mechnich, W. Braue, and D. J. Green, 'Volcanic Ash-Induced Decomposition of EB-PVD $Gd_2Zr_2O_7$Thermal Barrier Coatings to Gd-Oxyapatite, Zircon, and Gd,Fe-Zirconolite', Journal of the American Ceramic Society, **96** (6) (2013)1958-1965.

Tables

Table 1: Processing Parameters of EB-PVD alumina on top of 7YSZ TBCs.

Runs	Substrate Temperature(°C)	Pressure (mbar)	Feeding rate (mm/min)	Beam power kW	Deposition time (min.)	Coating Thickness (µm)	Deposition rate (µm/min)
Run 1	890±5	$6*10^{-3}$	0.8	65	10	85±10	9
Run 2	775±5	$6*10^{-3}$	0.5	44	10	26±5	2.6
Run 3	780±10	$9*10^{-3}$	0.5	44	10	58±5	1.6
Run 4	810±10	$9*10^{-3}$	0.5	44	45	110±10	2.4

Table 2: Chemical Composition of CMAS 1, UCSB CMAS and Iceland Volcanic ash

CMAS/VA	Chemical Composition (Mol. %)								Crystalline phase	Melting Point, °C
	CaO	MgO	Al_2O_3	SiO_2	FeO	TiO_2	Na_2O	K_2O		
CMAS 1	24.7	12.4	11.1	41.7	8.7	1.6	-	-	Pyroxene + Anorthite	1225°C-1250°C
UCSB CMAS	35.3	9.6	6.9	48.1	-	-	-	-	Amorphous	1235°C-1240°C
Iceland Ash	12.6	6.4	7	49.3	17.9	4	2	0.7	Amorphous + some crystalline phases	1150°C

Table 1: Summary of CMAS 1 reaction phases at 1250°C after 5 min. (EDS analysis)

Time	Designation	Comp. Mol. %					Phase
		CaO	MgO	$AlO_{1.5}$	SiO_2	FeO	
5 min	Sp	0	28.1	57.9	0	14	Spinel
10 h	Sp	0	27.8	64.4	0	7.8	Spinel
5 min	An	22.1	0	35.7	42.2	0	Anorthite
10 h	An	21	0	37.7	41.3	0	Anorthite
5 min	g	23.9	5.2	7.7	17.4	24.4	glass
10 h	g	23.2	13.7	16.6	34.3	12.2	glass

Table 2: Summary of UCSB CMAS reaction zones at 1250°C after 5 min. (EDS analysis)

Time	Designation	Comp. Mol. %					Phase
		CaO	MgO	$AlO_{1.5}$	SiO_2	FeO	
5 min	Sp	22.9	2.7	32.1	42.3	0	Melilite
10 h	Sp	31.9	10.5	13.3	44.3	0	Melilite
5 min	An	14.6	0	54.9	30.4	0	Anorthite
10 h	An	23.9	0	35.2	40.9	0	Anorthite
5 min	g	31.3	8.2	15.8	44.7	0	glass
10 h	g	33.7	12	13.2	41	0	glass

Table 3 : Summary of Iceland ash reaction zones at 1250°C after 5 min (EDS analysis)

Time	Designation	Comp. Mol. %							Phase
		CaO	MgO	$AlO_{1.5}$	SiO_2	FeO	TiO_2	$NaO_{0.5}$	
5 min	Sp	0	24	60.3	0	15.7	0		Spinel
10 h	Sp	0	22	60.7	0	17.4	0		Spinel
5 min	Ps	0	0	0	0	88.1	11.9		Pseudobrookite
10 h	Ps	0	0	0	0	58.5	41.5		Pseudobrookite
5 min	An	12.4	4.2	35.3	39.9	3.7	0.4	4.0	Anorthite
10 h	An	15.4	0	30.6	50.3	1.7	0	1.8	Anorthite
5 min	g	10	4.8	20.7	54.4	7.2	2.9		glass
10 h	g	10.1	3.8	27.2	50.6	5.7	2.6		glass

Figures:

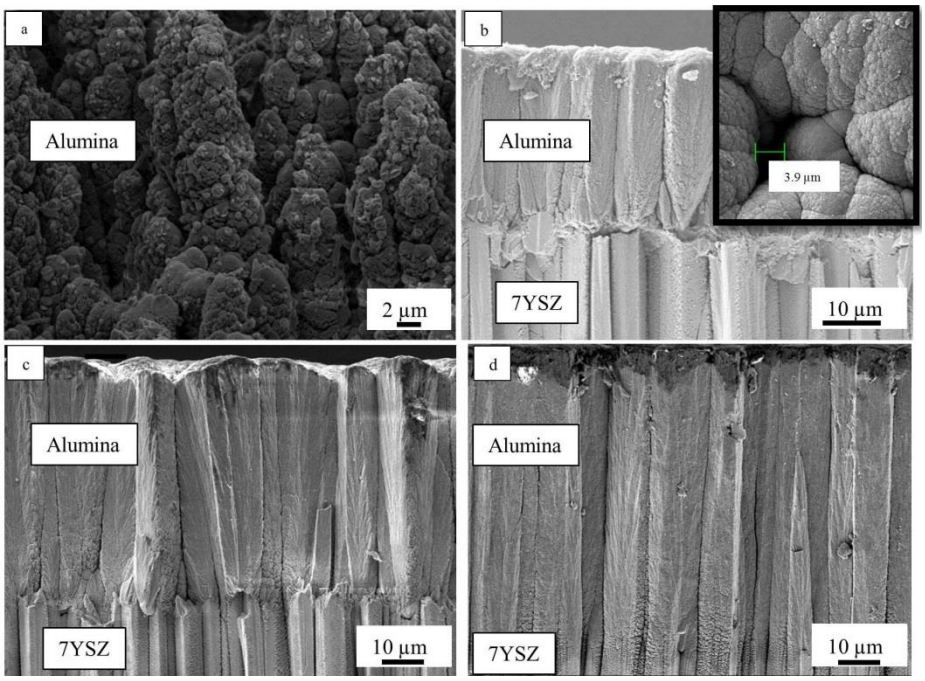

Figure 1: Fractured SEM micrographs of alumina/7YSZ EB-PVD coatings in as-coated conditions showing only the upper part of the 7YSZ layer, from (a) Run 1, (b) Run 2, (c) Run 3 and (d) Run 4. In set in (b) is the surface micrograph showing the presence of larger inter-columnar gap achieved in Run 2.

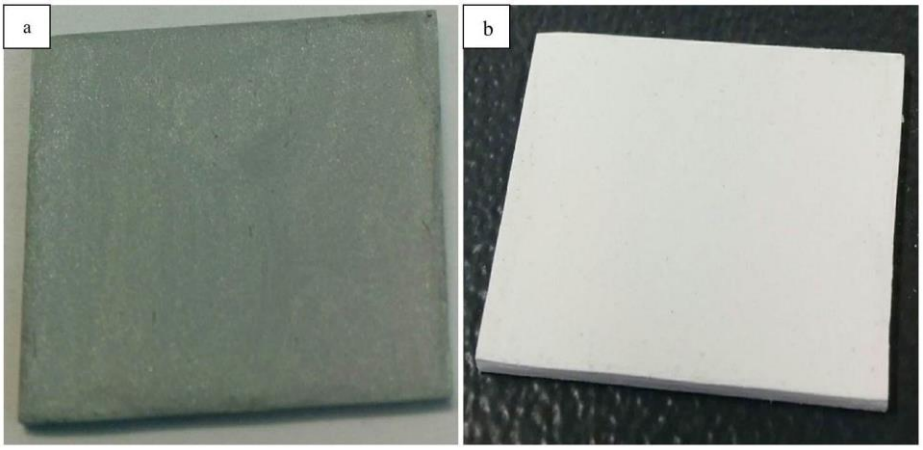

Figure 2: (a) RBAO precursor painted on top EB-PVD alumina, (b) RBAO coated surface after heat treatment.

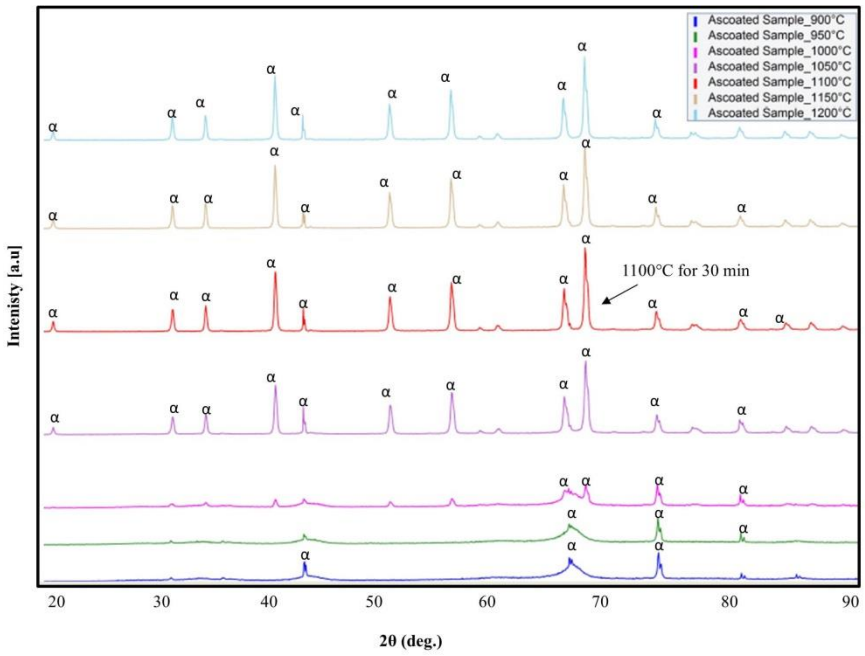

Figure 3: In-situ high temperature XRD patterns for as-coated alumina on EB-PVD 7YSZ coating on an alumina substrate. 1100°C peaks are only labelled with an arrow mark to convey the message that all the samples were annealed at this temperature and coating is purely crystalline in nature.

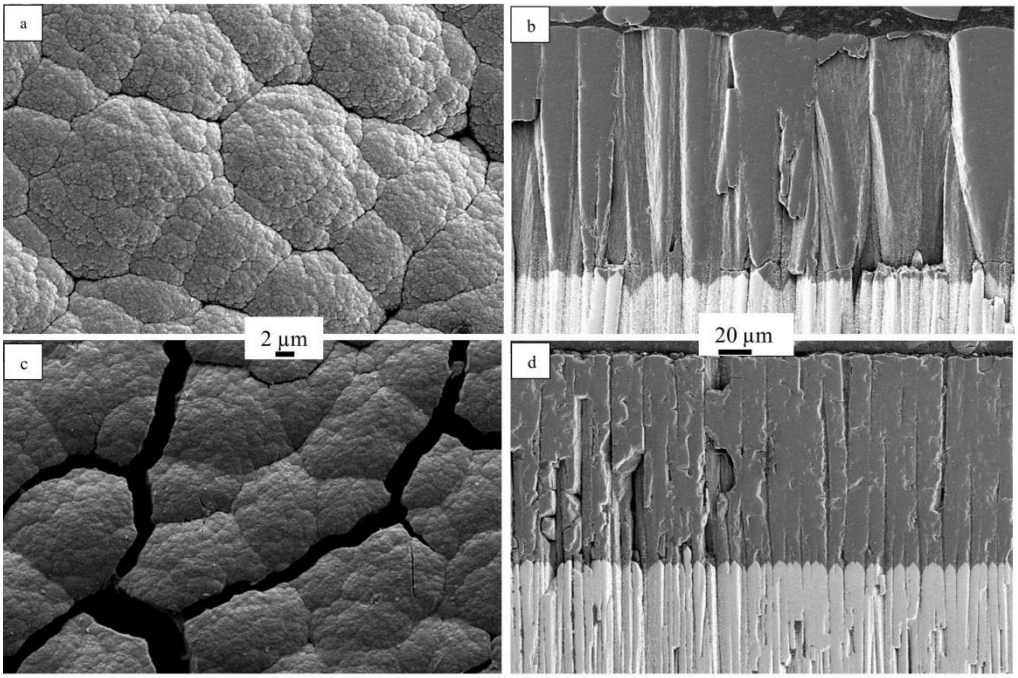

Figure 4: SEM micrographs taken on the top surface of the EB-PVD alumina coating, before (a) and after (c) the heat treatment at 1100°C for 30 min, (b) and (d) are the cross-sectional images of the Al_2O_3 coating after heat treatment. In (d) an area of a shrinkage cracks is shown while (b) represents a non-crack region showing a dense alumina coating.

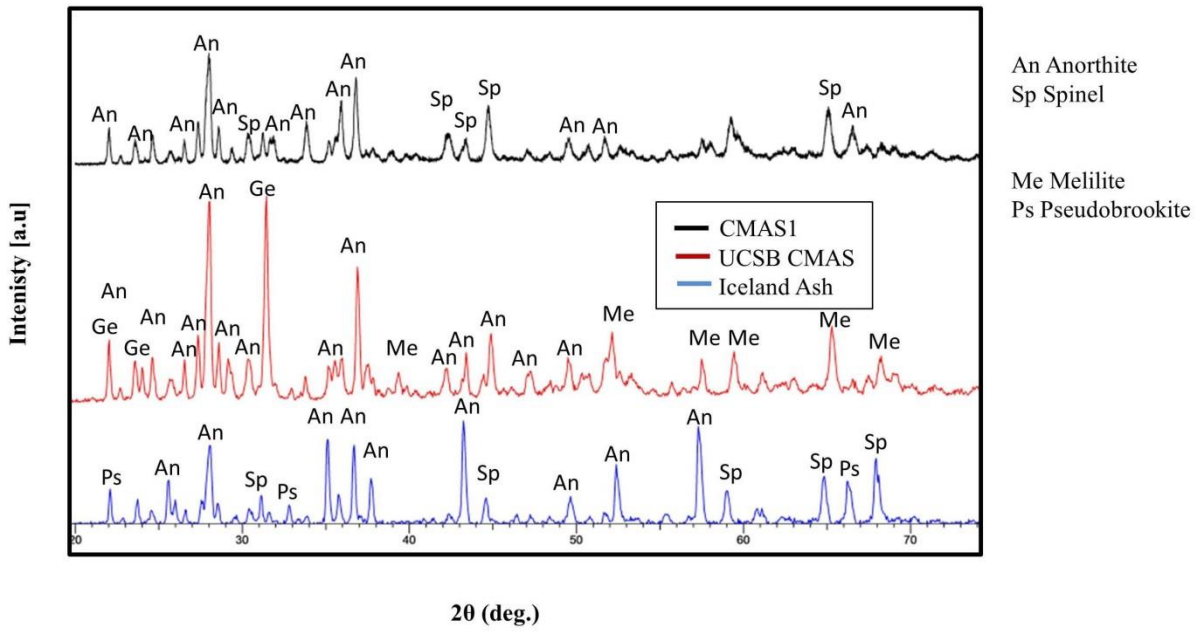

Figure 5: XRD patterns of CMAS/VA alumina mixtures after 10 h at 1250°C.

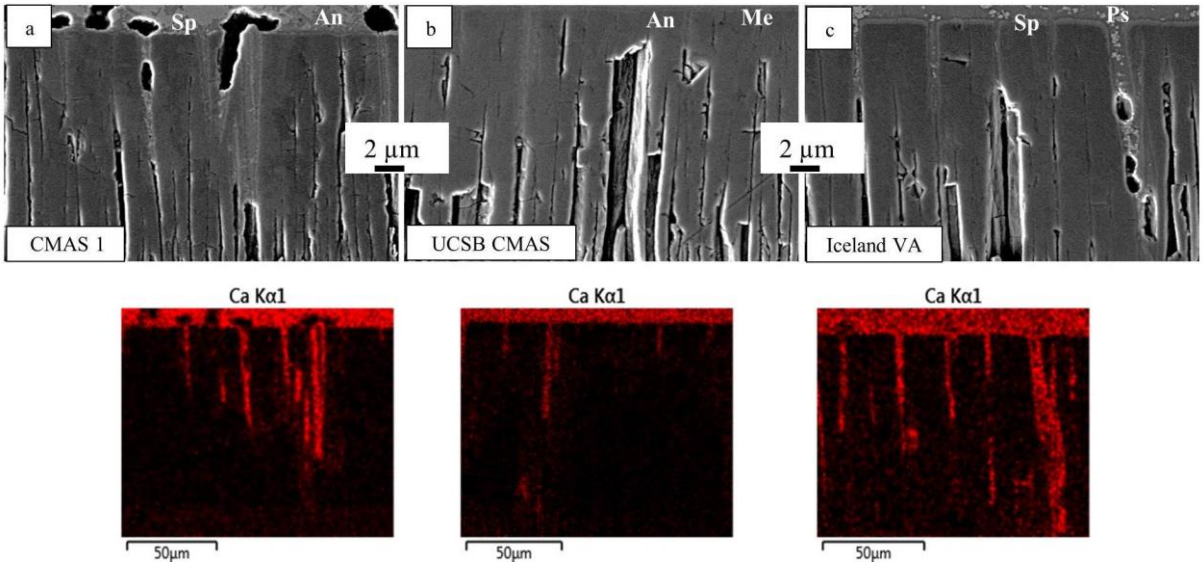

Figure 6: SEM cross sections of short term infiltration tests on EB-PVD alumina with (a) CMAS 1, (b) UCSB CMAS and (c) Iceland ash at 1250°C for 5 min with corresponding Ca-EDS mapping images (lower pictures).

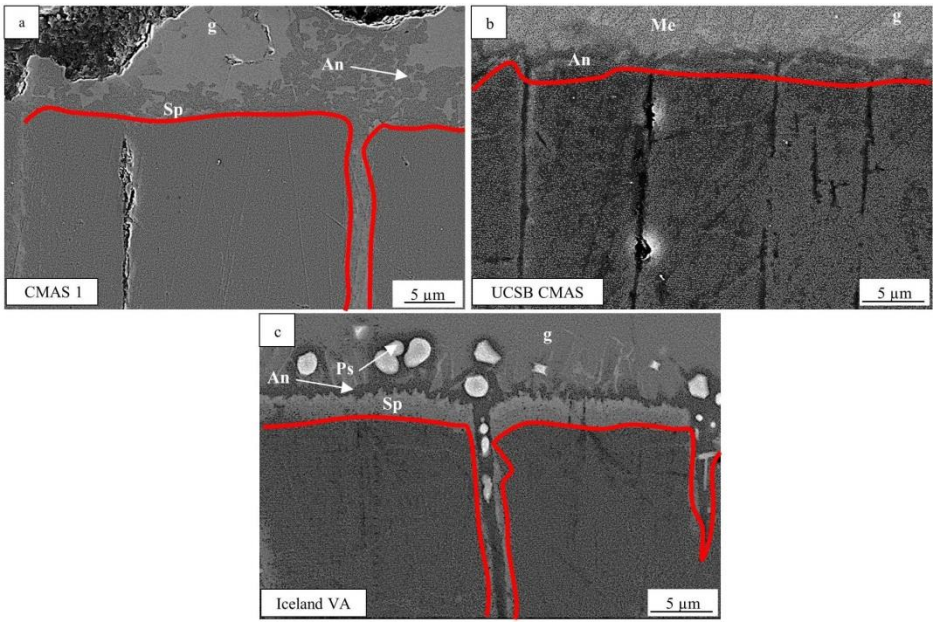

Figure 7: High magnification SEM micrographs showing the reaction layer (red lines are the boarders for the unreacted/reacted alumina) for (a) CMAS 1, (b) UCSB CMAS and (c) Iceland VA with EB-PVD alumina after 5 min. infiltration at 1250°C.

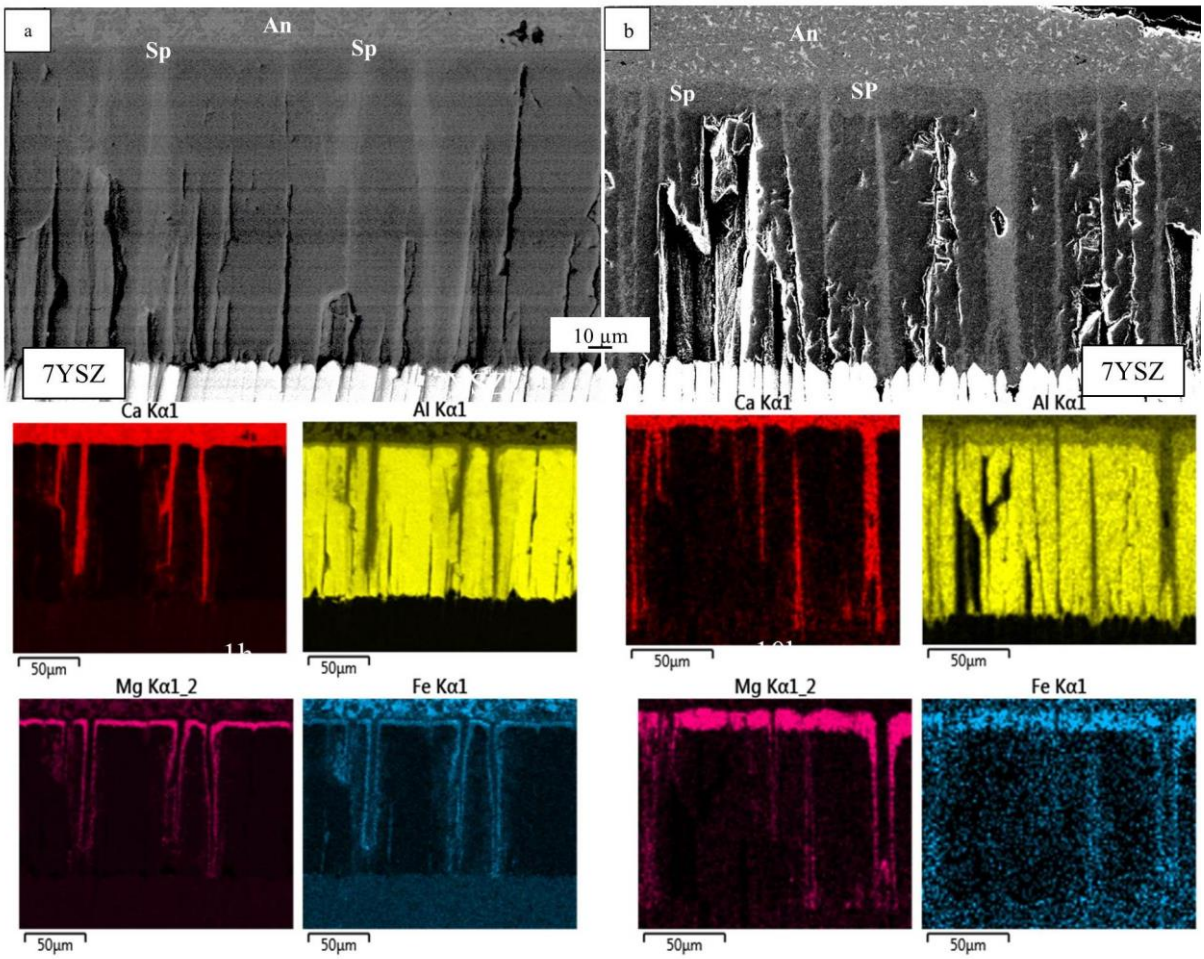

Figure 8: Elemental mapping of the reaction layer at the CMAS 1/alumina interface at 1250°C (a) after 1 h. and (b) after 10 h.

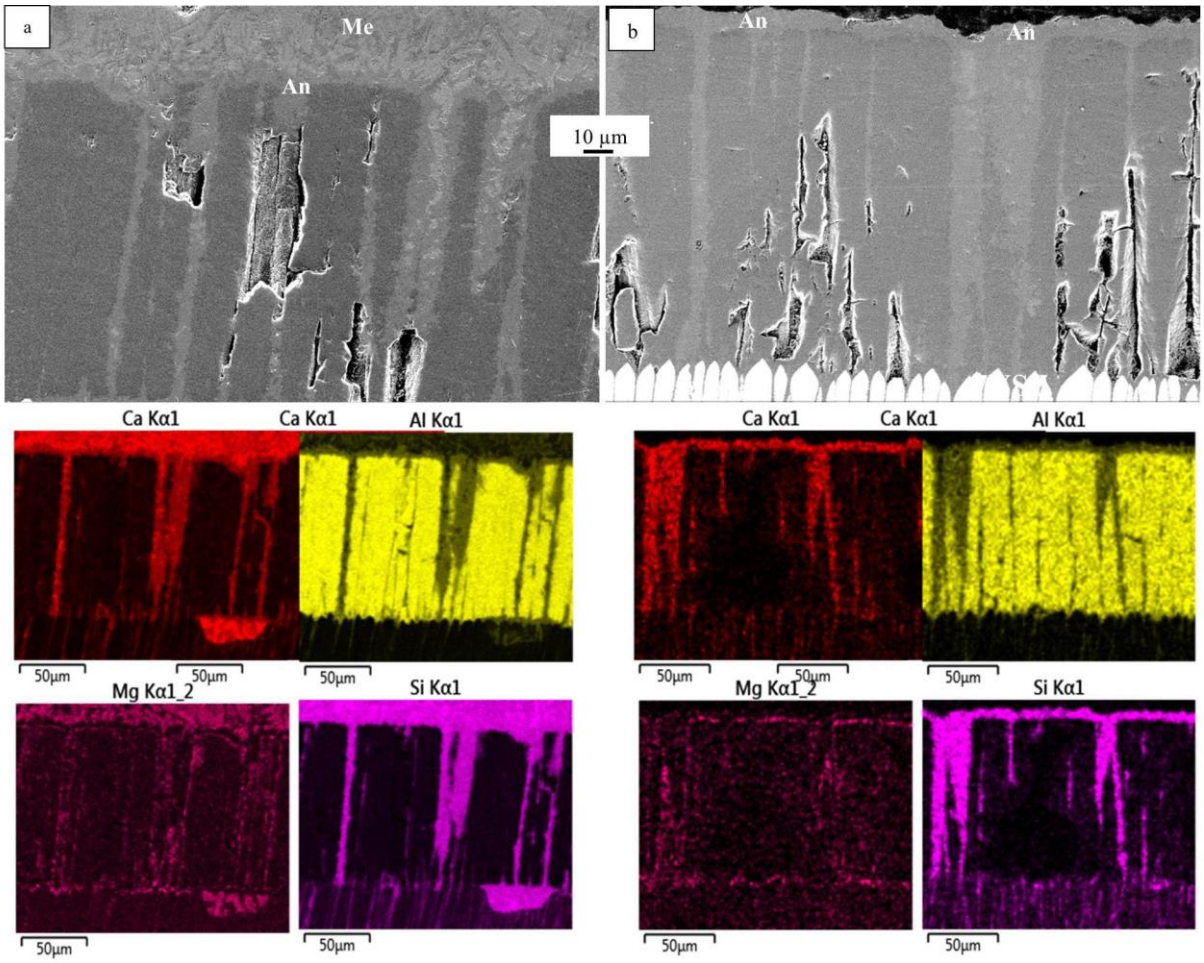

Figure 9: Elemental mapping of the reaction layer at the UCSB CMAS/alumina interface at 1250°C (a) after 1 h. and (b) after 10 h. see picture before, pl. correct all other figures as well, maybe adjust grey scale / brightness etc.

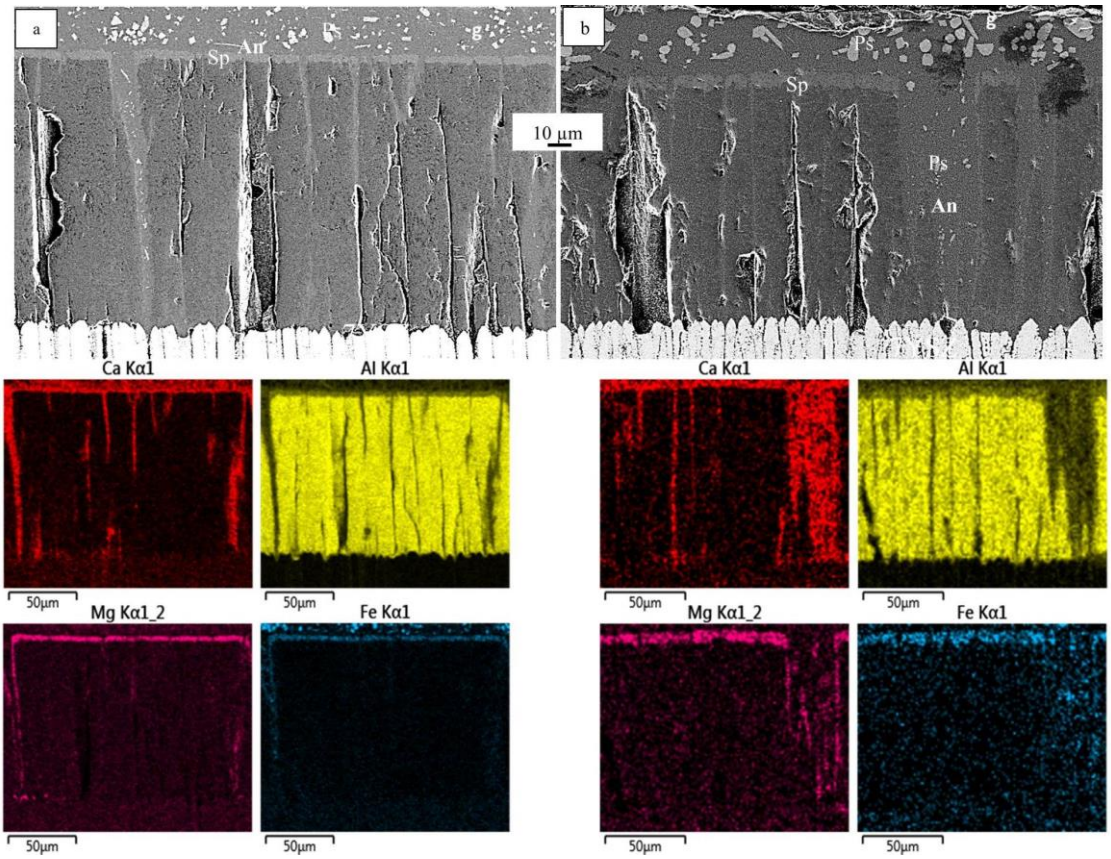

Figure 10: Elemental mapping of the reaction layer at the Iceland VA/alumina interface at 1250°C (a) after 1 h. and (b) after 10 h.

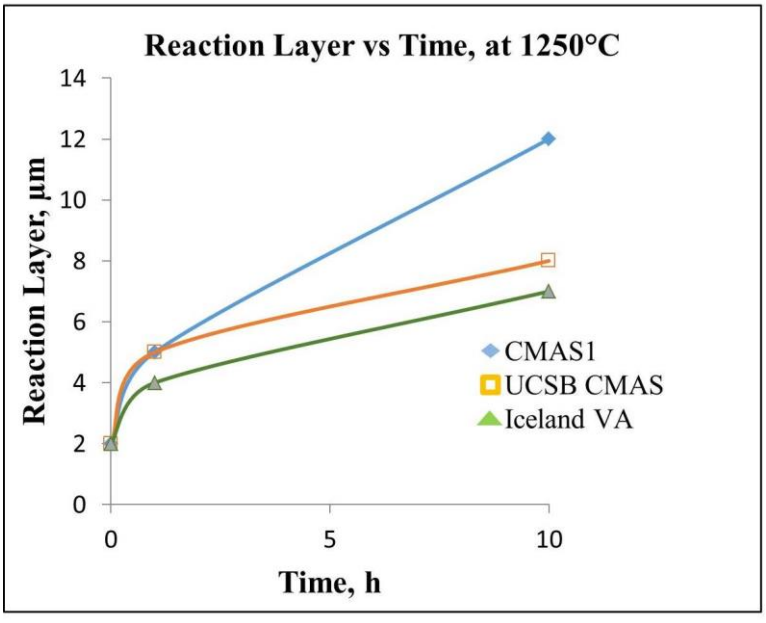

Figure 11: Progression of reaction layer on top of columns over time for isothermal tests at1250°C.

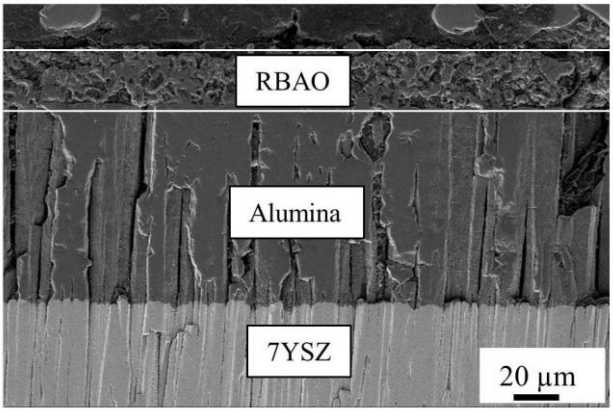

Figure 12: Cross section SEM micrograph of RBAO on top of EB-PVD Alumina/7YSZ.

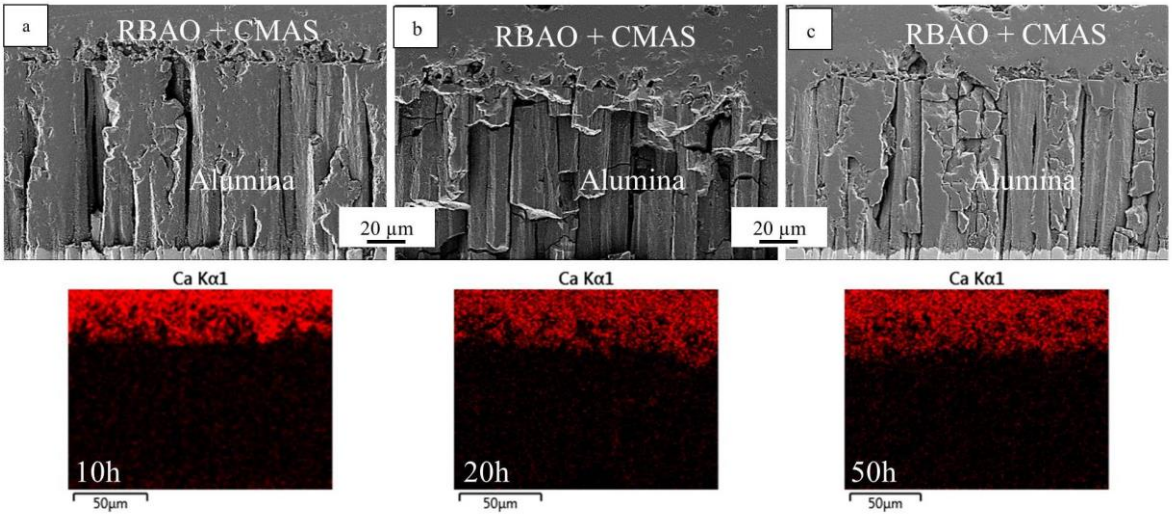

Figure 13: Elemental mapping of the reaction layer at the CMAS 1/ RBAO interface at 1250°C (a) after 10 h. and (b) after 20 h and (c) 50 h.

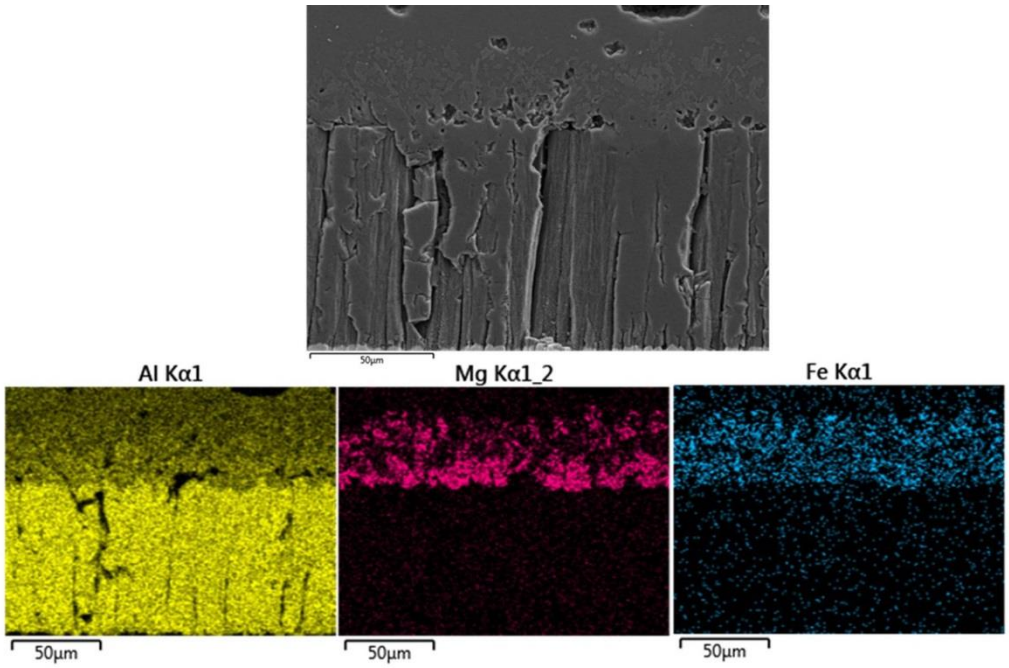

Figure 14: Elemental mapping of the reaction layer at the CMAS 1/ RBAO interface at 1250°C after 10 h.

Figure 15: Schematic representation of EB-PVD alumina reaction mechanism with CMAS 1, UCSB CMAS and VA at 1250°C after 5 mins (upper picture) and 10h (lower picture).